

# Supporting Information: A Systematic Study of $^{25}\text{Mg}$ NMR in Paramagnetic Transition Metal Oxides: Applications to Mg-ion Battery Materials

Jeongjae Lee<sup>1</sup>, Ieuan D. Seymour<sup>1</sup>, Andrew J. Pell<sup>2</sup>, Siân E. Dutton<sup>3</sup>, and Clare P. Grey<sup>1</sup>

<sup>1</sup>Department of Chemistry, Lensfield Road, Cambridge CB2 1EW, United Kingdom

<sup>2</sup>Department of Materials and Environmental Chemistry, Stockholm University, Svante  
Arrhenius Väg 16 C, SE-106 91 Stockholm, Sweden

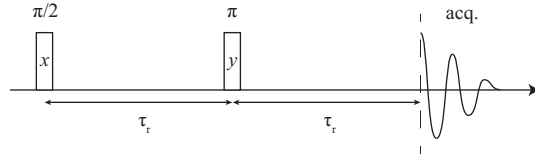
<sup>3</sup>Cavendish Laboratory, J. J. Thomson Avenue, Cambridge CB3 0HE, United Kingdom

## S1 DFT Population Analysis Data

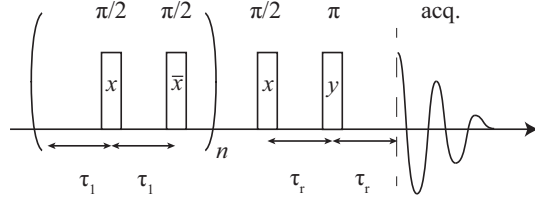
	$d_{xy}$	$d_{yz}$	$d_{zx}$	$d_{x^2-y^2}$	$d_z^2$
MgV <sub>2</sub> O <sub>4</sub>	0.625	0.625	0.625	0.056	0.056
MgMn <sub>2</sub> O <sub>4</sub>	0.934	0.934	0.919	0.143	0.855

Table S1: Mulliken spin population analysis of transition metal  $d$  orbitals in selected spinel compounds.

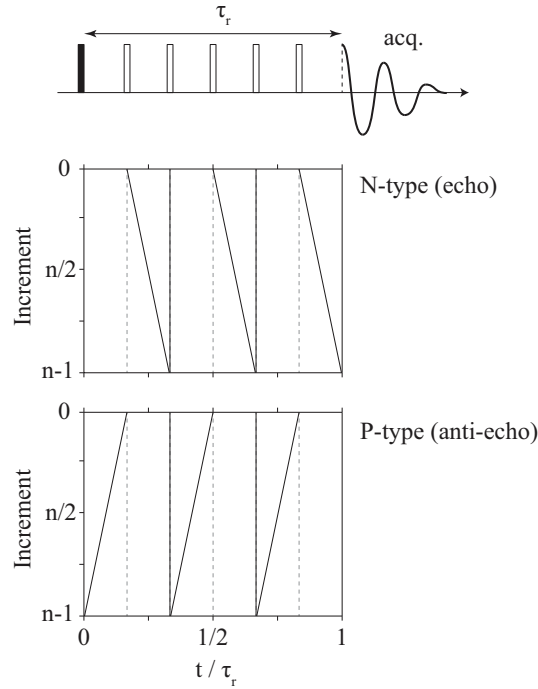
## S2 Pulse Sequences



(a) Rotor synchronized spin echo, with  $\tau_r$  being the rotor period.



(b) Rotor Assisted Population Transfer (RAPT), where the saturation frequency is given as  $\nu = 1/(2\tau_1)$ .



(c) Magic Angle Turning (MAT). Recoupling time which equals a full rotor period  $\tau_r$  was used to minimize loss in signal due to paramagnetic relaxation. Pulses at  $2/6\tau_r$  and  $4/6\tau_r$  were fixed and the timings of the other pulses are shifted according to echo or anti-echo types as shown.

Figure S1: Illustrations of pulse sequences used in this study.

All spin echo experiments, including those included in RAPT experiments, were performed with rotor-synchronized delays of  $71.42 \mu\text{s}$  (14 kHz MAS) and 0.1 s recycle delay. Lengths of RAPT pulses were calculated from the expression  $1/2\nu_m - \tau_1$ , where  $\nu_m$  is the RAPT modulation frequency and  $\tau_1 = 200 \text{ ns}$  is a short delay between the two pulses, allowing the transmitter to stabilize. 60 RAPT pulses ( $n = 30$ ) were applied to saturate the satellite levels.

### S3 DFS enhancement

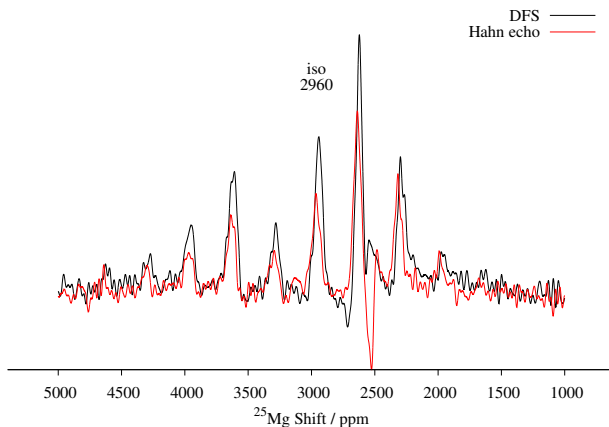


Figure S2:  $^{25}\text{Mg}$  NMR spectra of  $\text{Mg}_6\text{MnO}_8$ , recorded with rotor-synchronized Hahn echo and Double Frequency Sweep (DFS) pulse sequences. Signal-to-noise enhancement of around 1.5 is observed for the isotropic shift. A 36 kHz-strength DFS sweep pulse starting from an offset of 1000 kHz and ending at 100 kHz was applied for 2040  $\mu\text{s}$ . 51200 transients were acquired in each case with recycle delays of 0.01 s.

### S4 Euler Angle Conventions

Rotation matrix for converting column vectors in ZYZ convention, utilizing positive (counterclockwise) rotations:

$$\begin{bmatrix} x' \\ y' \\ z' \end{bmatrix} = \begin{bmatrix} \cos \alpha \cos \beta \cos \gamma - \sin \alpha \sin \gamma & \sin \alpha \cos \beta \cos \gamma + \cos \alpha \sin \gamma & -\sin \beta \cos \gamma \\ -\cos \alpha \cos \beta \sin \gamma - \sin \alpha \cos \gamma & -\sin \alpha \cos \beta \sin \gamma + \cos \alpha \cos \gamma & \sin \beta \sin \gamma \\ \cos \alpha \sin \beta & \sin \alpha \sin \beta & \cos \beta \end{bmatrix} \begin{bmatrix} x \\ y \\ z \end{bmatrix}$$

## S5 XRD Characterization Data

$R_{exp}$  refers to the expected  $R$ -factor and  $R_{wp}$  refers to the weighted  $R$ -factor against the observed intensity.

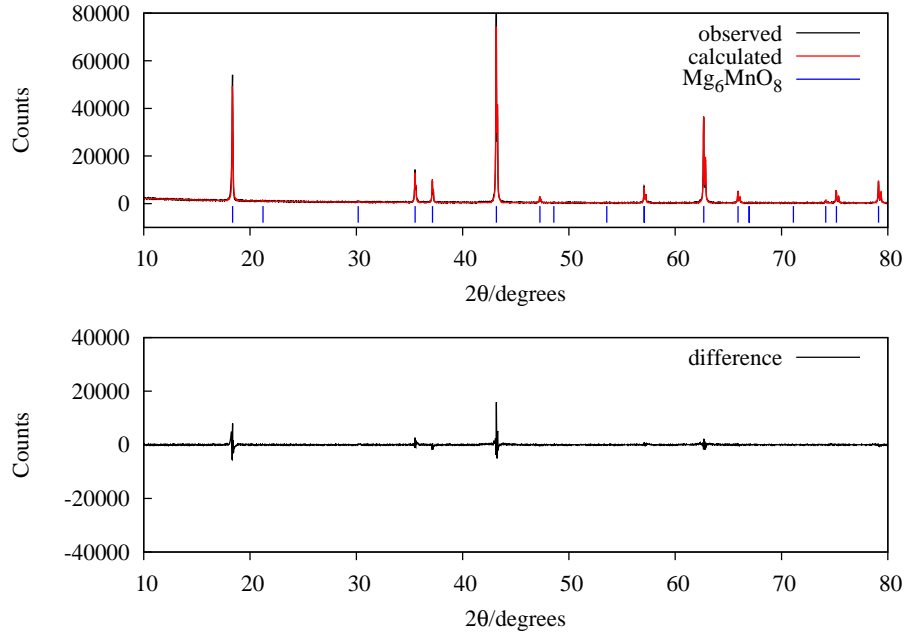


Figure S3: X-ray diffraction pattern for  $\text{Mg}_6\text{MnO}_8$ . Collected data (red), modelled data (black line) and the difference (lower panel) are shown. The position of allowed reflections are indicated by the tick marks.

$\text{Mg}_6\text{MnO}_8$ 100% $Fm\bar{3}m$ space group	
$a / \text{\AA}$	8.38008(6)
Mg1 (24d)	
$x$	0
$y, z$	0.25
occ	1
$B_{iso}$	1
Mn1 (4a)	
$x, y, z$	0
occ	1
$B_{iso}$	1
O1 (8c)	
$x, y, z$	0.25
occ	1
$B_{iso}$	1
O2 (24e)	
$x$	0.2293(3)
$y, z$	0
occ	1
$B_{iso}$	1
$R_{exp}$	2.41
$R_{wp}$	14.21
Goodness-of-fit	34.75

Table S2: Structural parameters for  $\text{Mg}_6\text{MnO}_8$  as determined from room temperature X-ray powder diffraction.

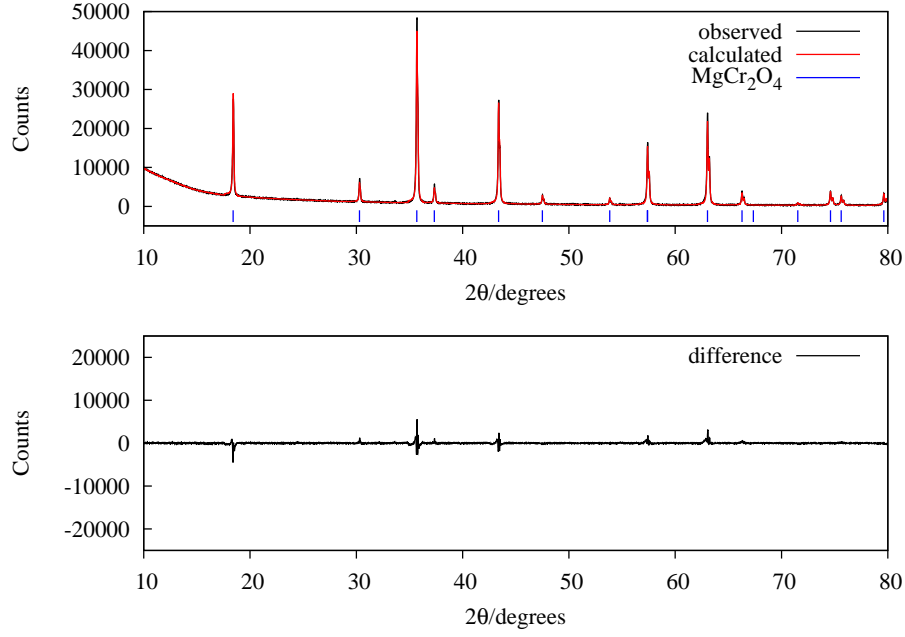


Figure S4: X-ray diffraction pattern for  $\text{MgCr}_2\text{O}_4$ . Collected data (red), modelled data (black line) and the difference (lower panel) are shown. The position of allowed reflections are indicated by the tick marks.

$\text{MgCr}_2\text{O}_4$  100 %  $Fd\bar{3}m$  space group

$a / \text{\AA}$	8.33242(9)
	Mg1 (8a)
$x, y, z$	0.375
occ	1
$B_{iso}$	0.39
	Cr1 (16d)
$x, y, z$	0
occ	1
$B_{iso}$	0.27
	O1 (32e)
$x, y, z$	0.2423(2)
occ	1
$B_{iso}$	0.38
$R_{exp}$	2.18
$R_{wp}$	7.70
Goodness-of-fit	19.93

Table S3: Structural parameters for  $\text{MgCr}_2\text{O}_4$  as determined from room temperature X-ray powder diffraction.

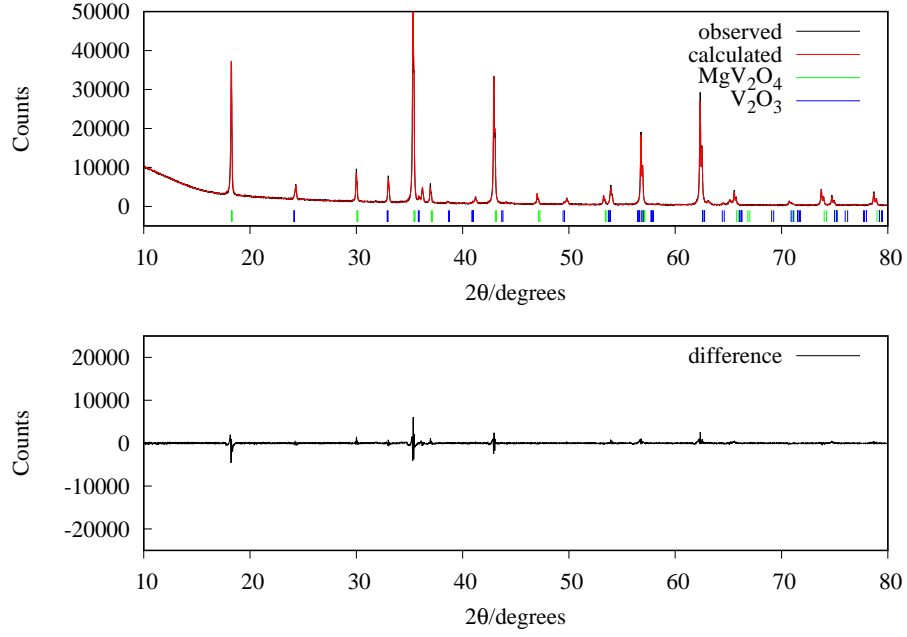


Figure S5: X-ray diffraction pattern for  $\text{MgV}_2\text{O}_4$ . Collected data (red), modelled data (black line) and the difference (lower panel) are shown. The position of allowed reflections are indicated by the tick marks. 15 % of  $\text{V}_2\text{O}_3$  was found in the sample.

$\text{MgV}_2\text{O}_4$ 84.6(4)%		$Fd\bar{3}m$ space group
$a / \text{Å}$		8.41719(8)
	Mg1 (8a)	
$x, y, z$		0.375
occ		1
$B_{iso}$		1.0
	V1 (16d)	
$x, y, z$		0
occ		1
$B_{iso}$		1.0
	O1 (32e)	
$x, y, z$		0.2426(1)
occ		1
$B_{iso}$		1.0
$R_{exp}$		2.37
$R_{wp}$		10.63
Goodness-of-fit		20.17

Table S4: Structural parameters for  $\text{MgV}_2\text{O}_4$  as determined from room temperature X-ray powder diffraction.

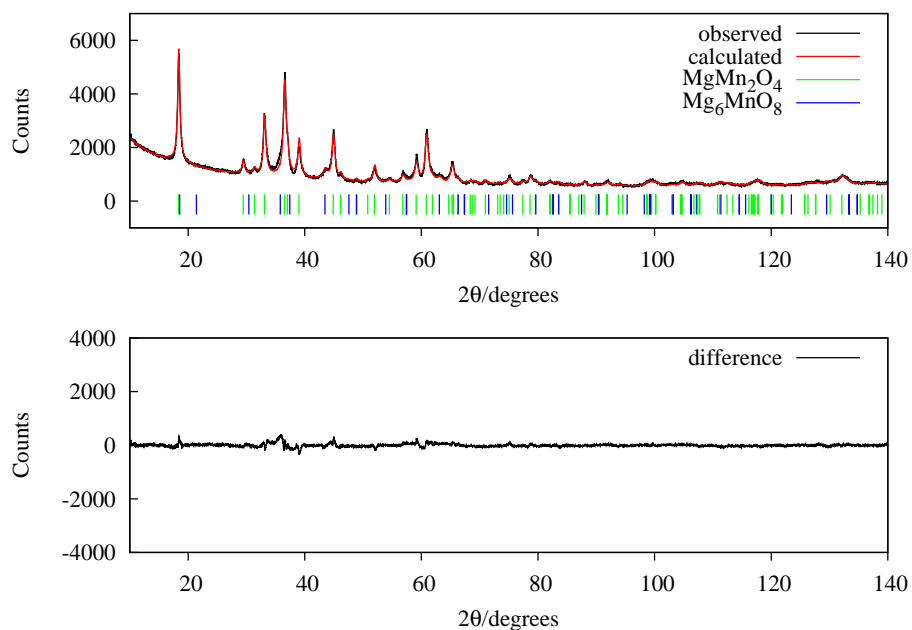


Figure S6: X-ray diffraction pattern for  $\text{MgMn}_2\text{O}_4$ . Collected data (red), modelled data (black line) and the difference (lower panel) are shown. The position of allowed reflections are indicated by the tick marks. 7.9 % of  $\text{Mg}_6\text{MnO}_8$  phase was detected.

$\text{MgMn}_2\text{O}_4$ 92.1(3)% $I41/amd$ space group	
$a / \text{\AA}$	5.7274(2)
$c / \text{\AA}$	9.2660(5)
Mg1 & Mn1 (4a)	
$x$	0
$y$	0.25
$z$	0.375
occ	0.91(1) & 0.09(1)
$B_{iso}$	0.5
Mn1 (8d)	
$x, y, z$	0
occ	1
$B_{iso}$	0.5
O1 (16h)	
$x$	0
$y$	0.51
$z$	0.2417(3)
occ	1
$B_{iso}$	0.5
<hr/>	
$R_{exp}$	3.28
$R_{wp}$	5.43
Goodness-of-fit	2.74

Table S5: Structural parameters for  $\text{MgMn}_2\text{O}_4$  as determined from room temperature X-ray powder diffraction.

## S6 Magnetic Characterization Data

$R^2$  refers to the coefficient of determination in the linear regression.

	$\mu_{eff}$ (SO) / $\mu_B$	$\mu_{eff}$ (expt) / $\mu_B$	$\Theta$ / K	$J_1$ / K	$T_N$ / K	Fitted range / K
$\text{Mg}_6\text{MnO}_8$	3.87	$3.99 \pm 0.01$	$-21.9 \pm 0.4$	$-0.73 \pm 0.01$	5	35–301
$\text{MgCr}_2\text{O}_4$	3.87	$4.25 \pm 0.03$	$-456.7 \pm 3.4$	$-30.4 \pm 0.2$	13	100–301
$\text{MgMn}_2\text{O}_4$	4.90	$5.93 \pm 0.06$	$-452.5 \pm 5.4$	–	–	200–301
$(\text{Mg}_{0.81}^{2+}\text{Mn}_{0.19}^{2+})\text{Mn}_2^{3+}\text{O}_4$	5.00					
$(\text{Mg}_{0.91}^{2+}\text{Mn}_{0.09}^{2+})\text{Mn}_2^{3+}\text{O}_4$	4.95					

Table S6: Magnetic characterization data of compounds studied.  $\mu_{eff}$  refers to the effective magnetic moment in Bohr magneton ( $\mu_B$ ) per TM ion,  $\Theta$  refers to the Weiss temperature,  $J_1$  refers to the nearest neighbor exchange coupling constant, and  $T_N$  refers to the Neel temperature. Theoretical spin-only values for the  $\text{MgMn}_2\text{O}_4$  compositions determined by phase fractions and occupancy refinements are also shown.

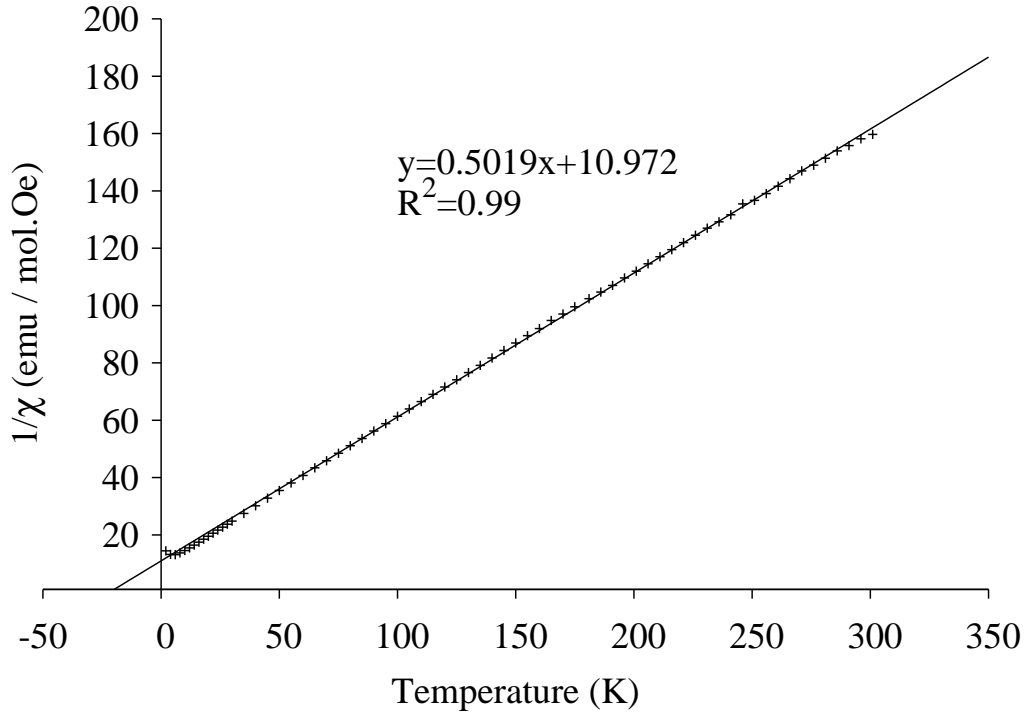


Figure S7: Inverse magnetic susceptibility per mol Mn,  $1/\chi$ , as a function of temperature for  $\text{Mg}_6\text{MnO}_8$ .

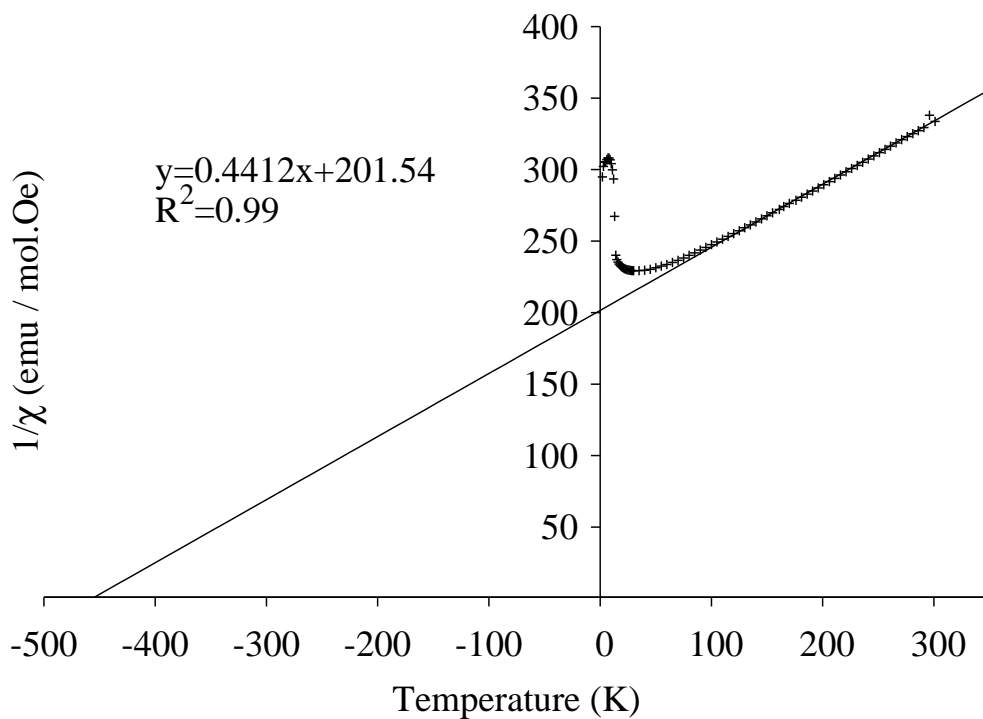


Figure S8: Inverse magnetic susceptibility per mol Cr,  $1/\chi$ , as a function of temperature for  $\text{MgCr}_2\text{O}_4$ .

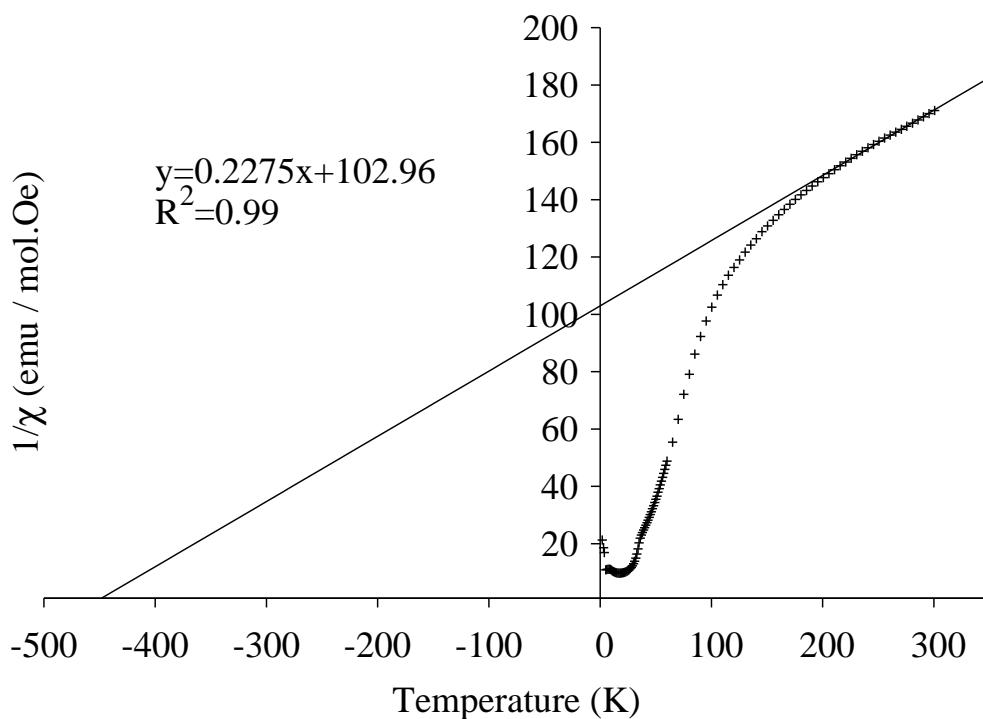


Figure S9: Inverse magnetic susceptibility per mol Mn,  $1/\chi$ , as a function of temperature for  $\text{MgMn}_2\text{O}_4$ .